IQGAP2 regulates blood-brain barrier immune dynamics

Ketaki A. Katdare[1], Andrew Kjar[2], Natasha M. O'Brown[3], Emma H. Neal[4], Alexander G. Sorets[2], Alena Shostak[5], Kate Mlouk[4], Hyosung Kim[4], Kensley B. Horner[4], Matthew S. Schrag[1,5,6], Sean G. Megason[3], Ethan S. Lippmann[1,2,4,5,6]

[1]Vanderbilt Brain Institute, Vanderbilt University, Nashville, TN, USA

[2]Department of Biomedical Engineering, Vanderbilt University, Nashville, TN, USA

[3]Department of Systems Biology, Harvard Medical School, Boston, MA, USA

[4]Department of Chemical and Biomolecular Engineering, Vanderbilt University, Nashville, TN, USA

[5]Department of Neurology, Vanderbilt University Medical Center, Nashville, TN, USA

[6]Vanderbilt Memory and Alzheimer's Center, Vanderbilt University Medical Center, Nashville, TN, USA

*Correspondence to Ethan S. Lippmann (ethan.s.lippmann@vanderbilt.edu)

Abstract

Brain endothelial cells (BECs) play an important role in maintaining central nervous system (CNS) homeostasis through blood-brain barrier (BBB) functions. In addition to actively regulating material exchange between the circulation and CNS, BECs express low baseline levels of adhesion receptors, which limits entry of leukocytes. Supporting cells in the neurovascular unit, such as astrocytes and pericytes, are crucial for promoting this immune privilege phenotype in BECs. However, the molecular mediators governing this phenotype are unclear. Here, we explored how BBB immune privilege is influenced by IQGAP2, a scaffold protein associated with elevated barrier function. Using single-cell RNA sequencing and immunohistology, we show that BECs from mice lacking Iqgap2 exhibit a profound inflammatory signature, including extensive upregulation of adhesion receptors and antigen-processing machinery. Further, in zebrafish and mice, loss of Iqgap2 increases infiltration of peripheral leukocytes into the brain. Overall, our results implicate IQGAP2 as an essential regulator of BBB immune privilege.

Introduction

Maintenance of central nervous system (CNS) homeostasis is crucial for ensuring normal functions in neurons and glial cells, which are sensitive to exogenous molecules in circulation [1,2]. The brain is insulated from these factors with the help of a specialized partition known as the blood-brain barrier (BBB). The BBB is composed of barrier-forming endothelial cells with unique cellular machinery that regulate the entry of macromolecules and solutes into the brain [3]. Brain endothelial cells (BECs) are equipped with transporters that control the bidirectional exchange of nutrients and waste and tight junctions that prevent passive leakage of blood components into the brain [4].

In addition to modulating molecular transport, BECs also act as a selective interface between the peripheral immune system and the brain [5]. Until recently, the CNS was considered to be completely isolated from the peripheral immune system and therefore an immune-privileged organ [6,7]. However, recent evidence shows that the CNS is under constant immune surveillance to identify and resolve mediators of injury [8,9]. For example, microglia are tissue resident innate immune cells that continually inspect the CNS parenchyma [10,11]. Further, although the CNS lacks a dedicated lymphatic system, interstitial fluid that perfuses the brain parenchyma through perivascular spaces, and cerebrospinal fluid that circulates through the ventricles and subarachnoid space, both provide drainage pathways for prospective antigens to reach the periphery and stimulate immune cells [12–15]. As such, initiation of an inflammatory response in the CNS is followed by recruitment of leukocytes to the target area across the BBB. BECs facilitate this process through the expression of various receptors, such as leukocyte adhesion molecules (LAMs), that allow interactions with and extravasation of leukocytes into tissue beds [16,17]. In addition, BEC chemokine signaling and antigen presentation [18–20] also play a key role in orchestrating leukocyte extravasation. While the underlying molecular mechanisms of leukocyte extravasation are similar across all organs, BECs have been shown to express very low levels of

LAMs at homeostasis making them refractory to mild inflammatory cues [2,21]. These properties suggest BECs are intrinsically different from peripheral endothelial cells in a manner that governs differential immune stimulation. However, despite several exquisite single-cell RNA sequencing (scRNA-seq) profiling studies identifying differentially expressed genes between BECs and peripheral endothelial cells [22–27], the molecular machinery responsible for this immune privilege in BECs has not been fully elucidated.

In this study, we used multiple model systems to demonstrate that IQGAP2, a scaffold protein historically viewed as a tumor suppressor [28–30], plays an important role in BBB immune privilege. Crucially, in mice, we demonstrate that global loss of Iqgap2 expression leads to upregulation of a multitude of inflammatory genes and signaling pathways in BECs that are involved in BBB-immune interactions. Further, in zebrafish and mice, we demonstrate that loss of Iqgap2 increases extravasation of peripheral leukocytes into the brain. Overall, our results benchmark IQGAP2 as a key molecular player involved in BBB immune privilege.

Results

Gene expression profiling in an iPSC-derived BBB model identifies IQGAP2 as a molecular factor associated with barrier tightness

In prior work, we have established protocols to differentiate human induced pluripotent stem cells (iPSCs) into BEC-like cells that exhibit hallmark BBB properties [31–34]. We further determined that retinoic acid (RA) signaling can profoundly enhance the barrier phenotype in iPSC-derived BEC-like cells [35,36]. To identify changes associated with this increase in barrier phenotype, we performed bulk RNA sequencing analyses on iPSC-derived BEC-like cells treated with vehicle control (DMSO), RA, or a retinoid X receptor agonist (CD3524) previously shown to induce a BBB phenotype similar to RA (Figure 1A). *IQGAP2* was identified as a significantly upregulated gene in response to both RA and CD3524 treatment (Figure 1B-C, Supplementary Figure 1, and Supplementary Tables 1 and 2), and we confirmed this outcome using qPCR (Figure 1D). Visualization of IQGAP2 in iPSC-derived BEC-like cells revealed widespread expression throughout cells, whereas IQGAP2 expression was sparse and perinuclear in non-barrier-forming human umbilical vein-derived endothelial cells (HUVECs) (Figure 1E). Using western blotting, we detected IQGAP2 protein expression in RA-treated BEC-like cells but not DMSO-treated BEC-like cells (Figure 1F). IQGAP2 was also expressed in barrier-forming Caco-2 epithelial cells, but not in endothelial cells that exhibit weak passive barrier function including HUVECs, immortalized human BECs (hCMEC/D3 line), and primary human BECs, which are known to rapidly de-differentiate after removal from the brain (Figure 1F) [37].

IQGAP2 is enriched in brain vasculature

To corroborate our *in vitro* findings *in vivo*, we analyzed IQGAP2 expression in primary mouse and human tissue samples. *IQGAP2* expression is not detected in BECs in several published

scRNA-seq datasets [22,25,38], but it is well-established that genes with low expression are difficult to detect by scRNA-seq [39]. Hence, we used more conventional methods to assess IQGAP2 expression in BECs. Using RT-PCR, we detected *Iqgap2* expression in mouse brain vasculature but not whole brain tissue from wild-type mice, and as expected, Iqgap2$^{-/-}$ mice lacked expression in both preparations (Figure 2A). We also confirmed Iqgap2 protein expression in cortices and microvessels isolated from wild-type but not Iqgap2$^{-/-}$ mice (Figure 2B). Protein expression analysis by immunohistochemistry (using a custom antibody raised against a peptide sequence specific to human IQGAP2) revealed robust IQGAP2 expression in the brain vasculature but not in the liver vasculature within post-mortem human tissues (Figure 2C). These findings indicate that IQGAP2 is expressed in brain vasculature, and the human tissue data indicate that IQGAP2 vascular expression may be selective to the brain.

Global loss of Iqgap2 yields a profound inflammatory transcriptomic profile in mouse BECs

In peripheral endothelial cells, Iqgap1 (homolog of Iqgap2) is essential for leukocyte extravasation [40,41]. Since IQGAP2 is believed to suppress the functions of IQGAP1 [42], and based on our data showing selective expression of IQGAP2 protein in human brain vessels, we hypothesized that IQGAP2 may be intrinsically responsible for BBB immune privilege and suppression of leukocyte extravasation. Further, IQGAP2 is a large scaffolding protein known to orchestrate many different cellular functions such as regulating cytoskeletal organization, cytokinesis. and carcinogenesis [43], suggesting it could govern intracellular outcomes along many different signaling axes to govern BBB identity. Having confirmed expression of Iqgap2 in brain vasculature (Figure 2), we sought to query this potential role for Iqgap2 by performing scRNA-seq on BECs from wild-type (WT) and Iqgap2$^{-/-}$ (KO) mice. To generate an endothelial cell-enriched population for sequencing, we isolated antibody-labeled CD31+ cells from dissociated mouse brains using

fluorescence-assisted cell sorting (Figure 3A). After implementing quality control metrics, cells were first analyzed using dimension-reduction by uniform manifold approximation and projection (UMAP) and unsupervised clustering to obtain 12 unique identities: endothelial cells (EC), PLVAP-expressing endothelial cells (EC_plvap), hemoglobin-expressing endothelial cells (EC_hb), endothelial/stromal cells or pericyte-like cells (EC/PC), endothelial/stromal cells or astrocyte-like cells (EC/AC), astrocytes (AC), B cells, T cells, monocytes (MNC), microglia (MG), oligodendrocytes (OLG) and fibroblasts (Supplementary Figure 2). Endothelial cells were the largest represented cell type, followed by immune cells such as monocytes and T cells that are predicted to also express CD31 (Figure 3B and Supplementary Figure 2); other cell types likely represent some small contamination in the sort. Each cell type was annotated using previously established marker genes [44] and all non-endothelial clusters were filtered out of the dataset for further analysis. Wild-type and Iqgap2$^{-/-}$ genotypes were equally represented in the EC cluster (Figure 3C), and bulk gene expression comparisons between WT and KO BECs show 928 differentially regulated genes (DEGs) (Figure 3D). Since leukocyte extravasation occurs predominantly at post-capillary venules [45–47], we examined these DEGs along the neurovascular tree. We used unsupervised clustering to subcluster BECs into 6 sub-populations, and based on marker gene expression, these subclusters were further classified into arterial (A; genes *Hey1, Bmx, and Sema3g*), capillary (C; genes *Slc16a2, Car4, and Mfsd2a*), and venous (V; genes *Icam1, Slc38a5, and Vwf*) zonal identities (Figure 3E and Supplementary Figure 2) [22]. Further analysis suggests that the strongest DEGs are shared among zonal identities and include genes involved in antigen presentation, interleukin receptor subunits, and adhesion molecules. Unique DEGs identified in the A and V zonal identities did not show any significant functional enrichment whereas a similar analysis of unique DEGs identified in the C zonal identity suggest subtle changes in BEC function (Figure 3F and Supplementary Table 3).

Across these zones, we were able to confirm that loss of Iqgap2 does not significantly affect expression of most canonical BBB genes, including junction proteins and nutrient transporters such as *Cdh5, Cldn5, Ocln, Tjp,* and *Slc2a1* (Supplementary Figure 3A). At the protein level, total vessel density was unchanged, and we found no obvious deficit in expression of claudin-5, occludin, ZO-1, and Glut1 in the Iqgap2$^{-/-}$ mice (Supplementary Figure 4). Additionally, we found significant differences in gene expression for certain transporters that facilitate exchange of amino acids and metabolites across the BBB, such as *Abcb1a*, *Slc7a1*, *Slc7a5*, and *Slc16a1* (Supplementary Figure 3B). Major regulator genes involved in BBB development and maintenance like *Mfsd2a* [48] and *Ctnnb1* [49–51] were also significantly downregulated in the Iqgap2$^{-/-}$ BECs, suggesting possible BBB dysfunction (Supplementary Figure 3C). Interestingly, we also saw significant upregulation of several LAMs and chemokine receptors. Although interaction with leukocytes and response to inflammation is primarily facilitated by venous ECs, we found that loss of Iqgap2 significantly upregulates expression of leukocyte receptors and signaling molecules like *Vcam1, Icam1,* and *Ackr1* across multiple vascular zones (Figure 4A). Using immunohistochemistry, we confirmed upregulation of Vcam1 in cortical vasculature of Iqgap2$^{-/-}$ mice (Figure 4B-C). The widespread expression of vascular Vcam1 in Iqgap2$^{-/-}$ mice was particularly striking, given that Vcam1 expression on BECs has been implicated in brain inflammation and cognitive decline in mice [52]. We have also recently shown that vascular VCAM-1 expression is significantly increased in Alzheimer's disease cortex relative to asymptomatic age-matched controls, further highlighting links to human neurodegeneration [53].

To extend our understanding of potential pathways affected by Iqgap2, we performed gene set enrichment analysis (GSEA) for KEGG signaling pathways. GSEA indicates that pathways involved in response to infections like Kaposi sarcoma-associated herpes virus infection (KSHV), human T-cell leukemia virus 1 infection (HTLV), human immunodeficiency virus 1 infection (HIV), and human papillomavirus infection (HPV) were upregulated. In addition, other pathways

facilitating immune interactions like cell adhesion molecules (*Vcam1, Icam1*), antigen processing and presentation (*Psme2, Hspa5, Canx, Calr*), and TNF signaling (*Cxcl1, Csf1, Ptgs2*) were also significantly upregulated in the Iqgap2$^{-/-}$ BECs (Figure 4D and Supplementary Figure 5). These results indicate that *Iqgap2* loss shifts both the transcriptional profile and protein expression of BECs towards an activated, inflammatory state.

Due to the significant upregulation of LAMs in the Iqgap2$^{-/-}$ BECs, we further analyzed cell-cell interactions between BECs and other cell types using CellChat [54]. We found that BEC-immune cell interactions were overrepresented in Iqgap2$^{-/-}$ mice. Quantification of these results suggested an increase in cell-cell interactions between BECs and microglia as well as BECs and peripheral immune cells like monocytes, T cells, and B cells. We then assessed the predicted directionality of these interactions by analyzing known receptor-ligand pairs. BECs were predicted to be the "senders" whereas immune populations, especially monocytes, were the primary "receivers" (Supplementary Figure 6). To understand whether these changes were due to Iqgap2 loss in a specific cell type, we performed DEG analyses in all clusters annotated as immune populations. We found a significantly higher number of DEGs in the monocytes as compared to other immune populations (Supplementary Figure 7A). KEGG pathway analysis of DEGs in the monocytes also indicates upregulation of pathways such as leukocyte transendothelial migration and regulation of actin cytoskeleton (Supplementary Figure 7B). These data indicate that Iqgap2 may also play an important role in modulating BEC-monocyte communication, which could additionally contribute to the overall inflammatory phenotype observed in the BECs in Iqgap2$^{-/-}$ mice.

Loss of Iqgap2 increases infiltration of peripheral immune cells into the brain in multiple organisms

Our scRNA-seq data suggest that Iqgap2 plays an important role in BBB immune privilege. To understand whether loss of Iqgap2 directly influences leukocyte infiltration into the CNS, we generated crispants by direct injection of Cas9 protein with multiple sgRNAs to target genes of interest in single-cell embryonic zebrafish with both endothelial cells (kdrl:mCherry) and immune cells (mpeg1:EGFP) transgenically labeled. We specifically assessed the presence of mpeg+ macrophage lineage cells in the brains of 5 dpf zebrafish that were either uninjected (UN) or targeting *tyr* or *iqgap2.* While uninjected fish are expected to retain normal function of all genes, *tyr* crispants should have mosaic knockout of tyrosinase*,* a protein involved in pigment production that is not expected to affect leukocyte infiltration; this serves as an additional control*.* As expected, both controls displayed similar numbers of mpeg+ cells in the brain, while *iqgap2* crispants displayed a significant increase in the number of mpeg+ cells (Figure 5B). Since mpeg also labels brain resident microglia, we used an established method to label microglia with Neutral Red dye [55] and distinguish these cells from infiltrating leukocytes. Uninjected controls and *iqgap2* crispants were therefore treated with Neutral Red and all mpeg+/Neutral Red+ double-positive microglia and mpeg+/Neutral Red- infiltrating leukocytes were quantified throughout the entire zebrafish brain. We measured a significant increase in the total number of mpeg+ cells, similar to previous experiments, but not double-positive microglia in the *iqgap2* crispants, and the number of mpeg+/Neutral Red- infiltrating leukocytes was significantly increased (Figure 5C). These data suggest that *iqgap2* is essential for restricting the infiltration of leukocytes into the CNS under homeostatic conditions, as its mosaic depletion enhanced the entry of peripheral leukocytes into the brain.

To assess whether murine Iqgap2 also influences leukocyte infiltration into the brain, we delivered IL1β into the lateral ventricles of wildtype and Iqgap2$^{-/-}$ mice to induce acute neuroinflammation [56,57]. After 24 hours, infiltration of leukocytes was assessed by immunohistochemical labeling of CD45+ cells in cortical brain sections. As expected, we measured an increase in the number

of CD45+ cells in the cortex of Iqgap2$^{-/-}$ mice as compared to their wildtype littermates (Figure 5D-E). We also confirmed that delivery of saline to the lateral ventricles in a similar fashion did not stimulate CD45+ cell infiltration into the brains of both wildtype and Iqgap2$^{-/-}$ mice (Supplementary Figure 8). These data suggest that Iqgap2 limits leukocyte infiltration into the mouse CNS following an inflammatory challenge.

Discussion

Peripheral endothelial cells display high levels of LAMs and can respond swiftly to local and systemic inflammatory cues [58]. This is followed by rapid infiltration of leukocytes into surrounding tissue beds. In comparison, BECs are immune quiescent under homeostatic conditions and generally express low levels of LAMs. This allows the BBB to more selectively control the activation of downstream inflammatory pathways and extravasation of leukocytes into the CNS [59,60]. Although peripheral immune responses are essential for the resolution of CNS injury, it is well established that age-related neurological deficits and chronic neurodegeneration may be exacerbated in part by unwarranted entry of leukocytes into the brain [61–65]. Further, BECs upregulate transcriptional signatures of inflammatory responses during aging and neurological disease [25,26,66]. As such, identifying mechanisms that regulate BEC inflammatory responses is critical for understanding the pathological progression of these diseases and developing strategies to decrease leukocyte extravasation.

To our knowledge, the role of IQGAP2 in BBB integrity has not been studied. *IQGAP2* belongs to the *IQGAP* family of scaffolding proteins involved in orchestrating a wide array of intracellular signaling and cytoskeleton dynamics [43]. The multidomain structure of these proteins acts as a framework for complex formation of signaling proteins, thus influencing many downstream cellular processes. *IQGAPs* were historically considered to be modulators of cytoskeletal architecture. However, it has become apparent that their role extends into other physiological processes like glomerular filtration in the kidney, cardiomyocyte function in the heart, and smooth muscle cell contraction in lung airways [43,67]. *IQGAP2* has been most notably studied in the context of its tumor-suppressive characteristics [29]. Previous studies identified *IQGAP2* as a novel tumor suppressor gene specifically linked to the development of hepatocellular carcinoma. More recently, *IQGAP2* inactivation has been linked to other malignancies like gastric cancer [68], prostate cancer [69], and bladder cancer [70]. Moreover, reduced expression of *IQGAP2* is

associated with worsened pathology and poor clinical outcomes [69,71,72]. Many of these studies also show that increased expression of *IQGAP1* carries similar pathology and clinical outcomes [73–75]. From these observations, it has been suggested that IQGAP1 and IQGAP2 may serve opposing functions [42]. This notion would be supported by our findings, since IQGAP1 is essential for leukocyte extravasation across peripheral endothelium [40,41], suggesting that the selective expression of IQGAP2 in BECs may serve to antagonize this role of IQGAP1.

One limitation of our study is that we cannot exclusively ascribe the observed *in vivo* phenotypes to loss of Iqgap2 expression in BECs. As IQGAP2 is predicted to be expressed in immune populations, we cannot discount the potential influence of immune-derived IQGAP2 signaling on the BEC phenotype. Our current data do suggest that cell-to-cell communication between BECs and monocytes may be bidirectional but is skewed towards BECs being the primary mediators of interactions. However, more extensive scRNA-seq profiling in immune cells, as well as lineage-specific Iqgap2 knockout models will be necessary in future studies to fully clarify cell-intrinsic effects of IQGAP2 on BBB immune privilege.

Another unaddressed aspect of our study is IQGAP2's mechanism of action. As a large scaffolding protein with several binding domains [43], IQGAP2 has the potential to orchestrate multiple cellular functions in diverse contexts. One known interaction with relevance to BBB function is with β-catenin [76], given that Wnt/β-catenin signaling is crucial for BBB development and maintenance [49–51]. Further, modulation of β-catenin expression in BECs in adult mice can profoundly influence BEC inflammation and CNS leukocyte infiltration [77]. In particular, one study using the experimental autoimmune encephalomyelitis model demonstrated that deregulation of Wnt/β-catenin signaling specifically in BECs increased vascular Vcam1 expression concurrent with increased infiltration of CD4+ T cells. As such, we envision future studies assessing connections between β-catenin, IQGAP2, and associated inflammatory phenotypes.

Last, a lingering question is whether IQGAP2 plays a role in human neurodegenerative disease progression. We did not observe any obvious differences in vascular IQGAP2 expression in brain sections from Alzheimer's disease patients versus age-matched asymptomatic controls (data not shown), but these evaluations were qualitative, and we did not have access to tissue from young donors for comparison. A more rigorous evaluation of vascular preparations from various human cohorts could ultimately provide insight into this question. Taken together, our collective data suggest that IQGAP2 plays an important and previously unrecognized role in maintaining BBB integrity and regulating immune cell trafficking to the CNS, and future work will determine cell-specific effects and relevance to human brain disorders.

Methods

Cell culture

iPSC maintenance: CC3 [78] iPSCs were maintained in E8 medium [79] on growth factor reduced Matrigel (Corning). iPSCs were passaged upon reaching 60-80% confluence using Versene (Gibco). iPSCs were not used beyond passage 45.

Caco-2 maintenance: Caco-2 cells were cultured on a 0.1% gelatin coating and maintained in DMEM containing glucose, pyruvate, and L-glutamine (Corning) supplemented with 1X- MEM non-essential amino acids (Sigma-Aldrich) and 10-20% heat-inactivated fetal bovine serum (Gibco). Caco-2 cells were passaged upon 80-90% confluence with TrypLE Express (Gibco).

Human umbilical vein endothelial cell (HUVEC) maintenance: HUVECs were cultured in 6-well plates coated with 0.1% gelatin. Cells were maintained in EBM-2 media (Lonza) with the full growth kit (Lonza) and passaged using TrypLE Express.

hCMEC/D3 maintenance: hCMEC/D3 cells were cultured on plates coated with 0.04 mg/mL Rat Tail Collagen I (Gibco) coated plates. Cells were maintained in EndoGRO-MV Complete Culture Media Kit (Sigma) supplemented with 0.2 ng/mL bFGF. Once confluent, cells were passaged using TrypLE Express.

Human brain microvascular endothelial cell (hBMEC) maintenance: Primary hBMECs were purchased from Sciencell and cultured on Rat Tail Collagen I coated plates using EGM-2 medium. Once confluent, cells were passaged using TrypLE Express.

Differentiation of iPSCs to BEC-like cells: CC3 iPSCs were differentiated into BEC-like cells using previously described protocols [33]. iPSCs were seeded onto Matrigel-coated plates at a density of 15,800 cells/cm^2 in E8 medium containing 10 μM Y27632 (Tocris). The next day, cells were switched to E6 medium [31] to induce differentiation. Cells were cultured in E6 medium for 4 days

with daily media changes. On the fourth day of differentiation, the medium was changed to complete endothelial cell medium (EC medium) composed of human endothelial serum-free medium (hESFM, Gibco) with 200X B27 (Gibco), 400X GlutaMAX (Gibco), and 20 ng/mL basic fibroblast growth factor (bFGF, Peprotech). Media was additionally supplemented with 10 μM all-trans retinoic acid (RA, Sigma Aldrich), 10 μM CD3254 (Tocris), or an equal volume of DMSO (Sigma Aldrich). Following a 48-hour incubation in each condition, cells were washed with 1X DPBS (Gibco), dissociated into a single-cell suspension using StemPro Accutase (Gibco), and collected via centrifugation. Cells were resuspended in complete EC medium and plated onto tissue culture treated plates or Transwell filters coated with collagen IV (400 μg/mL, Sigma Aldrich) and fibronectin (100 μg/mL, Sigma Aldrich). 24 hours later, media was changed to fresh EC medium containing no bFGF or RA, CD3254 or DMSO. Transendothelial electrical resistance (TEER) was measured 24 hours later using an EVOM2 with STX2 chopstick electrodes (World Precision Instruments) to confirm expected phenotypes.

Zebrafish maintenance and procedures

Zebrafish were maintained at 28.5°C following standard protocols [80]. All zebrafish work was approved by the Harvard Medical Area Standing Committee on Animals under protocol number IS00001263-3. Adult fish were maintained on a standard light-dark cycle from 8 am to 11 pm. Adult fish, aged 3 months to 2 years, were crossed to produce embryos and larvae. For imaging live larvae, 0.003% phenylthiourea (PTU) was used beginning at 1 day post fertilization (dpf) to inhibit melanin production. These studies used the AB wild-type strains and the transgenic reporter strains (Tg(kdrl:HRAS-mCherry)^{s896} [81], abbreviated as Tg(kdrl:mCherry), and Tg(mpeg1:EGFP)^{gl22} [82], abbreviated as Tg(mpeg1:EGFP). Mosaic *iqgap2* crispants were generated by injection of 7 μM Cas9 protein complexed with four sgRNAs (5'-AGTAGCCTCGATTTACAGG-3', 5'-GCACTTTGTCAGTCACGGAA-3', 5'-CAGGAC

AGCGCGAGCACTG-3', and 5'-AAAGTCCGCGCGCAGTTTA-3') to target multiple sites in the *iqgap2* transcript, and *tyr* control crispants were similarly targeted with four sgRNAs (5'-GCCGCACACAGAGCCGTCGC-3', 5'-GGATGCATTATTACGTGTCC-3', 5'- GACTCTACATCG GCGGATGT-3', and 5'-GTATCCGTCGTTGTGTCCGA-3'). To distinguish between microglia and macrophages, 4 dpf larvae were exposed to 2.5 µg/ml of Neutral Red (Millipore Sigma: N7005) in embryo water for 3 hours at 28.5°C. Larvae were washed at least three times to remove the residual dye and then microglia were assessed the next day as previously described[55]. Zebrafish larvae were immobilized by tricaine exposure and live imaged on a Leica SP8 line scanning confocal microscope. Quantification of mpeg+ and Neutral Red+ cells was manually performed on blinded z-stack images that spanned the entire larval head using ImageJ.

Mouse maintenance and procedures

Colony maintenance: All mouse protocols were approved by the Institutional Animal Care and Use Committee at Vanderbilt University under protocol number M200049-00. Iqgap2$^{-/-}$ mice (129S background) were obtained from Jackson Laboratory (strain 025452). Male and female Iqgap2$^{-/-}$ mice and wild-type littermate controls were used for all experiments. Mice were at least 8 weeks of age at the time of use and were housed continuously in an environmentally controlled facility in a 12-hour light/dark cycle with *ad libitum* access to food and water.

Genotyping: Mice were ear-tagged and tail snips were collected at approximately 2 weeks of age. Genomic DNA was extracted using an Extracta DNA Prep kit for tissue (Quantabio) per manufacturer instructions. DNA was extracted in the Extraction buffer at 95°C for 30 minutes, cooled to room temperature and mixed with Stabilization buffer before being stored at -20°C. The reactions were performed using the Apex Hot Start Taq BLUE Master Mix (Apex Bioresearch) on a ProFlex PCR system (Applied Biosystems). A touchdown cycling protocol was used with an

initial annealing temperature of 65°C gradually lowered to 60°C over the course of 10 cycles. Genotyping primers used were as follows: Mutant Reverse–ATTTGTCACGTCCTGCACGACG, Wild-type Reverse–TGGCCTTCCTCCCTTAAAGT, and Common Forward–TGACTCAGAGGGCACATGGT. PCR products were run on a 2% agarose-TAE buffered gel supplemented with SYBR Safe DNA Gel Stain (Invitrogen) and imaged using a LI-COR Odyssey Fc gel imager (Supplementary Figure 9).

Tissue collection: Mice were deeply anesthetized using high-dose isoflurane and euthanized by transcardial perfusion of 1X DPBS (Gibco), followed by 4% paraformaldehyde (PFA, Thermo Fisher Scientific). Brains were extracted and postfixed in 4% PFA overnight followed by cryopreservation in sucrose gradient solutions (15% and 30%, respectively). The tissue was then embedded in OCT medium (Tissue-Tek) and 15 µm thick sections were cut and stored at -80ºC.

Microvessel isolation: Mice were deeply anesthetized using high-dose isoflurane and euthanized by decapitation. Brains were extracted and collected in ice-cold PBS. Microvessels from the cortex were isolated as previously described[83]. In brief, cortices were dissected from remaining brain tissue, homogenized in PBS using a tissue homogenizer (Wheaton), and collected by centrifugation. Homogenized tissue was resuspended in a 15% dextran solution (~70,000 kDa, Sigma) and centrifuged at 10,000xg to separate the vessel fraction from the remaining tissue. The vessel fraction was washed with PBS and filtered using a 40 µm cell strainer (Corning). For RNA extraction, the vessel fraction was resuspended in TriZOL (Invitrogen) and RNA was extracted using a Direct-zol RNA prep kit (Zymo Research) and stored at -80ºC. RNA concentration was quantified using a NanoDrop (Thermo Fisher Scientific). For protein extraction, the vessel fraction was incubated in RIPA buffer (Sigma) supplemented with 1% v/v protease and phosphatase inhibitor cocktails (Sigma) for 30-60 minutes on ice. Cell debris was separated by centrifugation (12,000xg for 15 minutes at 4ºC) and the supernatant was stored at -20ºC. Protein concentration

was quantified using a Pierce BCA Protein Assay (Thermo Fisher Scientific) according to the manufacturer instructions.

Intracerebroventricular injection of IL1β: Male and female Iqgap2$^{-/-}$ mice and wild-type littermates were used as experimental animals. All animals were at least 12 weeks old at the time of the surgery. Under isoflurane anesthesia, mice were unilaterally injected into the lateral ventricle using a stereotactic apparatus at coordinates of AP = -0.3 mm, ML = -1 mm, and DV = -3 mm. After injections, mice were returned to prewarmed home cages for recovery. Each mouse received 20 ng/μL of IL1β solution (20 ng in 1 μL PBS). 24 hours after surgery, mice were transcardially perfused with PBS followed by 4% paraformaldehyde and brains were extracted for immunohistological analysis. In a separate control cohort, we delivered 1 μL saline to Iqgap2$^{-/-}$ and wild-type mice by intracerebroventricular injection and performed immunohistochemical analysis in a similar manner to confirm that post-surgical inflammation did not elicit recruitment of CD45+ cells to the brain at the equivalent time point. For quantification, CD45+ cells were manually counted in each section under blinded conditions. Vasculature was labelled using fluorescently labelled lectin (Vector labs) to ensure that CD45+ cells had extravasated out of the vessels into the brain parenchyma.

Human tissue

De-identified brain tissue was obtained from the Vanderbilt Brain and Biospecimen Bank at Vanderbilt University Medical Center. Written consent for brain donation was obtained from patients or their surrogate decision makers. All brain tissue collection procedures were approved by the Institutional Review Board at Vanderbilt University Medical Center. Normal liver tissue samples were provided by the NCI Cooperative Human Tissue Network (CHTN). All tissue specimens were fixed overnight in 4% PFA, cryopreserved in gradient sucrose solutions (15%

followed by 30% solution), and embedded in OCT medium (Tissue-Tek). Tissue specimens were cryosectioned and stored at -80°C. All acquired images were processed and quantified using ImageJ software. For quantification of vascular IQGAP2, mean IQGAP2 intensity was calculated within CD31+ vessels.

Polymerase chain reaction assessment of mouse tissue

RNA from cortex or isolated microvessels (1 µg/sample) was reverse-transcribed to cDNA using a cDNA High Capacity Reverse Transcription Kit (Applied Sciences) without RNase inhibitor according to manufacturer instructions. 9 µL of cDNA was used to prepare the PCR reaction mix according to standard Taqman Gene Expression Assay protocol (Life Technologies) with Taqman primers (Iqgap2: Mm01282601_m1, Cldn5: Mm00727012_s1, Gapdh: Mm99999915_g1). Using a Biorad CFX96 thermocycler, cDNA was amplified for 40 cycles (denaturing: 95°C for 15 seconds, annealing and extension: 60°C for 30 seconds). PCR products were examined by gel electrophoresis using 4% Ultrapure agarose (Fisher Scientific) gels supplemented with SYBR Safe DNA gel stain (Invitrogen).

Quantitative polymerase chain reaction assessment of cultured cells

Cells were washed with 1X DPBS and incubated in Accutase until detached. Cells were collected via centrifugation, resuspended in TriZOL, and stored at -80°C. RNA was extracted using an RNeasy Mini Kit (Qiagen). RNA was quantified using a Qubit Fluorometer (Thermo Fisher Scientific) and a Qubit RNA BR assay kit (Thermo Fisher Scientific). cDNA was generated using a cDNA High Capacity Reverse Transcription Kit (Applied Sciences) without RNase inhibitor according to manufacturer instructions. PCR reaction mixes were prepared according to standard Taqman Gene Expression Assay protocol (IQGAP2: Hs01117929_m1, GAPDH:

Hs02786624_g1). Using a Biorad CFX96 thermocycler, cDNA was amplified for 40 cycles (denaturing: 95°C for 15 seconds, annealing and extension: 60°C for 30 seconds).

RNA isolation and bulk sequencing

Purified iPSC-derived BEC-like cells cultured on 6-well plates were washed once with DPBS, collected using a cell scraper (Fisher Scientific) in an additional 1 mL of DPBS, and pelleted via centrifugation. Cell pellets were resuspended in TRIzol and stored at -80°C until the day of isolation. On the day of isolation, RNA was isolated according to manufacturer's instructions using a Direct-zol Miniprep kit (Zymo Research) with DNase I treatment. All samples were isolated concurrently to prevent batch-to-batch variability. Isolated samples were submitted to Vanderbilt Technologies for Advanced Genomics (VANTAGE) facility for sequencing using an Illumina NovaSeq6000. Raw data was processed through a bulk RNAseq pipeline in accordance with the Snakemake (5.2.4) workflow management system [84]. Quality control monitoring was done with FastQC v0.11.8 before and after quality and adapter trimming, as performed by Trim Galore v0.5.0. Trimmed paired-end sequences were aligned to the human genome (GRC38) with STAR 2.60c, utilizing Gencode genomic feature annotations (v26). Following quantitation, feature counts were used for all downstream analysis. Differential gene expression between RA vs DMSO and CD3254 vs DMSO was determined based on gene counts and sample metadata using DESeq2 [85].

Western blotting

Cultured cells were washed with 1X DPBS and scraped off the plate using a cell lifter (VWR) or enzymatically dissociated with Accutase or TrypLE Express. Cells were then incubated in RIPA buffer supplemented with 1% v/v protease and phosphatase inhibitor cocktails for 30-60 minutes

on ice. Protein was quantified using a Pierce BCA Protein Assay according to manufacturer instructions. Protein samples from cultured cells or mouse tissue were prepared by diluting 20-40 µg of protein with 1X Laemmli buffer (Biorad) supplemented with beta-mercaptoethanol (Sigma) and Ultrapure water (Gibco) to a final volume of 20-30 µL. Samples were then boiled at 95ºC for 5 minutes, cooled on ice, and centrifuged briefly. Samples were then loaded into 4-20% Criterion TGX Midi protein gels (Biorad) along with Precision Plus Dual Color Protein ladder (Biorad) and run at 80-120V. Protein gels were then transferred onto iBlot2 Nitrocellulose membranes (Thermo Fisher Scientific) using an iBlot2 transfer device (Thermo Fisher Scientific). Membranes were cut to size and blocked for at least 30 minutes at room temperature in Intercept TBS Blocking buffer (LI-COR Biosciences) on a shaker. Membranes were submerged in primary antibodies diluted in blocking buffer with 0.05% Tween20 (Sigma) and incubated at 4ºC overnight. Following primary antibody incubation, membranes were washed in wash buffer (1X tris buffered saline with 0.05% Tween-20). Membranes were incubated in secondary antibodies diluted in the wash buffer at room temperature for 2 hours. All primary and secondary antibody information is listed in Supplementary Table 2. Blots were imaged using a LI-COR Odyssey Clx or Fc Imager and bands were quantified using Image Studio Lite software.

Development of a custom antibody against human IQGAP2 protein

A peptide corresponding to amino acid residues 1460-1474 of human IQGAP2 (RSIKLDGKGEPKGAK) was synthesized with an amino-terminal cysteine and conjugated to maleimide-activated Keyhole Limpet Haemocyanin (KLH), maleimide-activated bovine serum albumin (BSA), and SulfoLink resin using manufacturer protocols (Thermo Fisher). The peptide-KLH conjugate was used to immunize rabbits (Cocalico Biologicals). Rabbit antisera were tested for the presence of antibodies recognizing the IQGAP2 peptide by dot blot analysis using the peptide-BSA conjugate. The rabbit antibodies were affinity-purified from the antisera using the

peptide-SulfoLink resin, where 5 mL of rabbit sera was diluted 1:1 with PBS and passed over a 2 mL peptide-SulfoLink column. After extensive washing with PBS, bound antibodies were eluted with 8.5 mL 0.1 M Glycine (pH 2.2) and collected in a tube containing 1.5 mL of 1 M Tris (pH 8). Antibody solution was stored at -80°C.

Immunofluorescent staining

Immunocytochemistry: Cells were washed with 1X DPBS and then fixed with 4% PFA for 10 minutes at room temperature. Blocking buffer was made with 1X PBS with 5% donkey serum (Sigma) or normal goat serum (Thermo Fisher Scientific), with or without 0.03% Triton X-100 (Sigma). Cells were incubated in an appropriate blocking buffer for at least 1 hour at room temperature. Cells were incubated in primary antibodies diluted in blocking buffer overnight at 4ºC. Afterwards, cells were washed with 1X PBS thrice for 5 minutes each. Appropriate secondary antibodies were diluted in 1X PBS and incubated with cells for 1 hour at room temperature. Cells were washed then with 1X PBS thrice for 5 minutes each and nuclei were counterstained with DAPI for 10 minutes at room temperature. All antibodies and corresponding dilutions used for immunocytochemistry are listed in Supplementary Table 2. Cells were then imaged using a Leica DMi8 epifluorescence microscope. All acquired images were processed using ImageJ software.

Immunohistochemistry: Tissue slices were retrieved from the -80ºC freezer and allowed to thaw at room temperature for 10-15 minutes. Sections were washed with 1X PBS with 0.03% Triton X-100 to remove the OCT medium. Human tissue sections were fixed with 4% PFA for 10 minutes at room temperature and then allowed to photobleach overnight on ice under a 240-watt LED panel with emissions at 390 nm, 430 nm, 460 nm, 630 nm, 660 nm, and 850 nm (GrowLight, HTG Supply Inc). Sections were then blocked and immunolabelled as described above. All antibodies and corresponding dilutions used for immunohistochemistry are listed in Supplementary Table 2.

Following final washes, tissue was mounted in Prolong Gold Antifade Mountant with DAPI (Invitrogen) and slides were allowed to dry overnight before imaging on a Leica DMi8 epifluorescence microscope. All acquired images were processed and quantified using ImageJ software. For quantification of vascular Vcam1 expression, mean Vcam1 intensity was calculated within CD31+ vessels.

Single-cell RNA sequencing

Fresh cortical tissue was homogenized and delipidated using an Adult Brain Dissociation Kit (Miltenyi Biotec) according to the manufacturer's instructions. The resultant single-cell suspension was incubated with TruStain FcX (Biolegend) for 10 minutes at 4°C to prevent non-specific antibody binding of Fc receptors, labeled with a secondary conjugated CD31 antibody (1:2000, eBioscience) for 30 minutes, and counterstained with DAPI. Live CD31+ cells were flow sorted using a 4-laser FACS Aria III sorter (BD Biosciences) at the Vanderbilt Flow Cytometry Shared Resource. Live cells were resuspended in DMEM (Gibco) supplemented with 2% FBS to obtain a concentration of 700-1200 cells/μL. RNA extraction, 10X Genomics Chromium 5' scRNAseq Library Prep, and sequencing on an Illumina NovaSeq6000 sequencer was performed at the VANTAGE core facility.

Single-cell RNA sequencing analysis

All gene by counts data were read into Seurat (v.4). The initial data were filtered to retain only cells with RNA counts between 1,200 and 20,000 (with less than 10% being mitochondrial). Within each biological experiment, data were log normalized. The top 2,000 variable features (as identified by variance) were selected. Samples were combined using CCA (Seurat v.4) and then standardized. UMAP based on the first 50 principal components was used to reduce

dimensionality for visualization and clustering [86]. Predicted doublets were filtered out using DoubletFinder [87]. Unsupervised clustering was achieved using the KNN-graph approach in Seurat [88], and clusters were annotated with SingleR [89] based on previously published datasets [44]. Predominantly endothelial clusters (0,2,4,5) were rescaled and clustered based on the first 15 principal components. Clusters were annotated as arterial, capillary, or venous based on the expression of established marker gene sets [22]. Approximately 2,000 ECs were analyzed per condition. Differentially expressed genes (DEGs) were computed in Seurat using the FindMarkers() function with built-in Bonferroni correction. KEGG or Reactome gene set enrichment analysis (GSEA) was computed on significant DEGs using WebGestalt with a false discovery rate cutoff of 0.05 and weighted set cover redundancy reduction [90]. Communication between cell types was predicted using the CellChat R packages [54]. For visualization, *EnhancedVolcano* [91], *UpSetR* shiny app [92], *iGraph* [93], and *ggvenn* were employed. Full code is available at: https://github.com/LippmannLab/IQGAP2_WT_KO_BEC_scRNAseq.

Statistical analysis

Statistical analysis for scRNA-seq data was conducted in R. All other analysis was performed in GraphPad Prism 9.0.0.

Data availability

Bulk RNA-seq data can be accessed at Array Express under accession number E-MTAB-12678. scRNA-seq data can be accessed at ArrayExpress under accession number E-MTAB-12687.

Author contributions

KAK, ESL, and EHN conceived the study. KAK and ESL designed the majority of experiments with input from the other authors. KAK, NMO, EHN, AGS, and AS conducted all experiments. AK performed all bioinformatics analyses. KM assisted with data quantification. HK provided assistance with human tissue histology. KBH provided animal husbandry support. MSS provided human tissue samples. SGM assisted NMO with experimental planning and data interpretation.

Acknowledgments

Funding was provided by a Chan Zuckerberg Initiative Ben Barres Early Career Acceleration Award (grant 2019-191850 to ESL). AK and EHN were supported by the National Science Foundation Graduate Research Fellowship Program. NMO was supported by a Damon Runyon Postdoctoral Fellowship. Support for RNA sequencing was provided by Vanderbilt Technologies for Advanced Genomics core facility, which is supported by the CTSA Grant (NIH grant 5UL1 RR024975), the Vanderbilt Ingram Cancer Center (NIH grant P30 CA68485), the Vanderbilt Vision Center (NIH grant P30 EY08126), and NIH/NCRR grant G20 RR030956. Support for histology was provided by Vanderbilt Translational Pathology Shared Resource core facility, which is supported by P30 CA068485. Flow Cytometry experiments were performed in the VMC Flow Cytometry Shared Resource, which is supported by P30 CA068485 and the Vanderbilt Digestive Disease Research Center (P30 DK058404). The custom IQGAP2 antibody in this study was produced by Vanderbilt Antibody and Protein Resource, which is supported by P30 CA068485. Support for bulk RNA-seq analyses was provided by Creative Data Solutions, a Vanderbilt shared resource. The authors thank Dr. Jose Gomez and Sarah Sturgeon for early assistance with the Iqgap2$^{-/-}$ mice and Dr. Eric Shusta for sharing microarray data that initially indicated the potential relevance of IQGAP2 in iPSC-derived BEC-like cells. Some figures in this manuscript were created in part using BioRender.

Competing interests

The authors declare no competing interests.

Figures

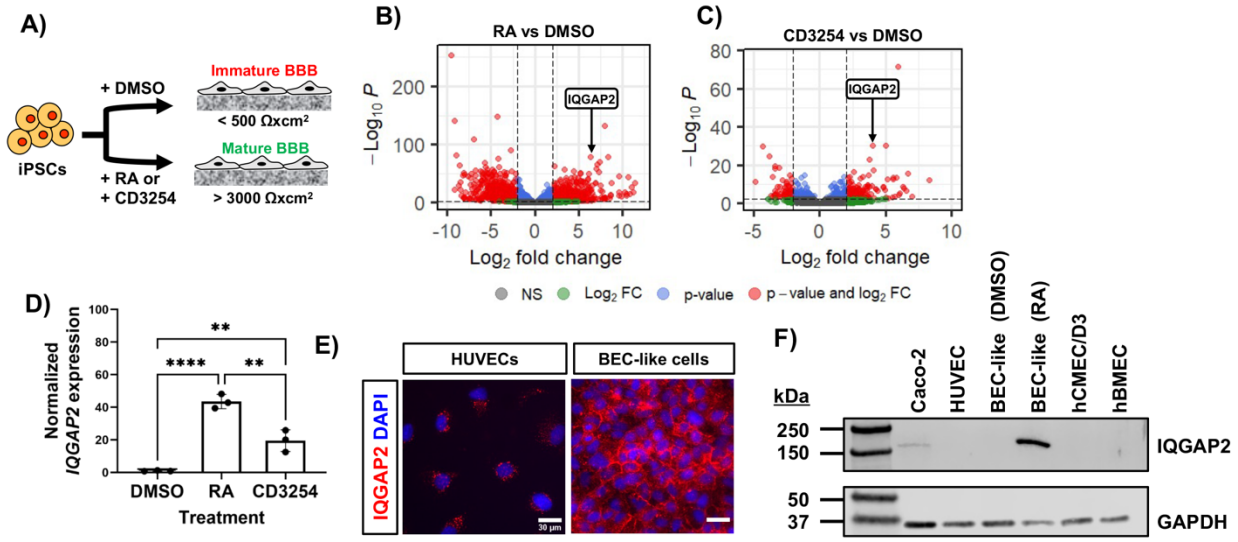

Figure 1: IQGAP2 expression correlates with barrier phenotype in cultured cells.

A) Schematic representation of experimental design for bulk RNA-seq analyses. Human iPSCs were differentiated into BEC-like cells in the presence of barrier enhancing molecules (RA or CD3254) and vehicle control (DMSO) to yield a mature or immature BBB phenotype, respectively.

B) Volcano plots highlighting differentially expressed genes across RA and DMSO treatment in iPSC-derived BEC-like cells. Non-significant genes are labelled in grey, genes with >2-fold change are labelled in green, $p<0.05$ are labelled in blue, and $p<0.05$ and >2-fold change are labelled in red. Analyses are based on N=3 biological replicates per condition.

C) Volcano plots highlighting differentially expressed genes across CD3254 and DMSO treatment in iPSC-derived BEC-like cells. Non-significant genes are labelled in grey, genes with >2-fold change are labelled in green, $p<0.05$ are labelled in blue, and $p<0.05$ and >2-fold change are labelled in red. Analyses are based on N=3 biological replicates per condition.

D) Quantitative PCR assessment of *IQGAP2* expression in iPSC-derived BEC-like cells after RA, CD3254, or DMSO treatment. N=3 biological replicates per condition. Data represented as mean ± SD. *GAPDH* was used as the housekeeping gene. Statistical significance was calculated using a one-way ANOVA with Tukey's multiple comparison's test (**, $p<0.01$; ****, $p<0.0001$).

E) Representative immunofluorescence images of IQGAP2 expression in HUVECs and iPSC-derived BEC-like cells treated with RA.

F) Western blot of IQGAP2 expression across different cultured human cell lines and primary sources. Data are representative of N=3 biological replicates.

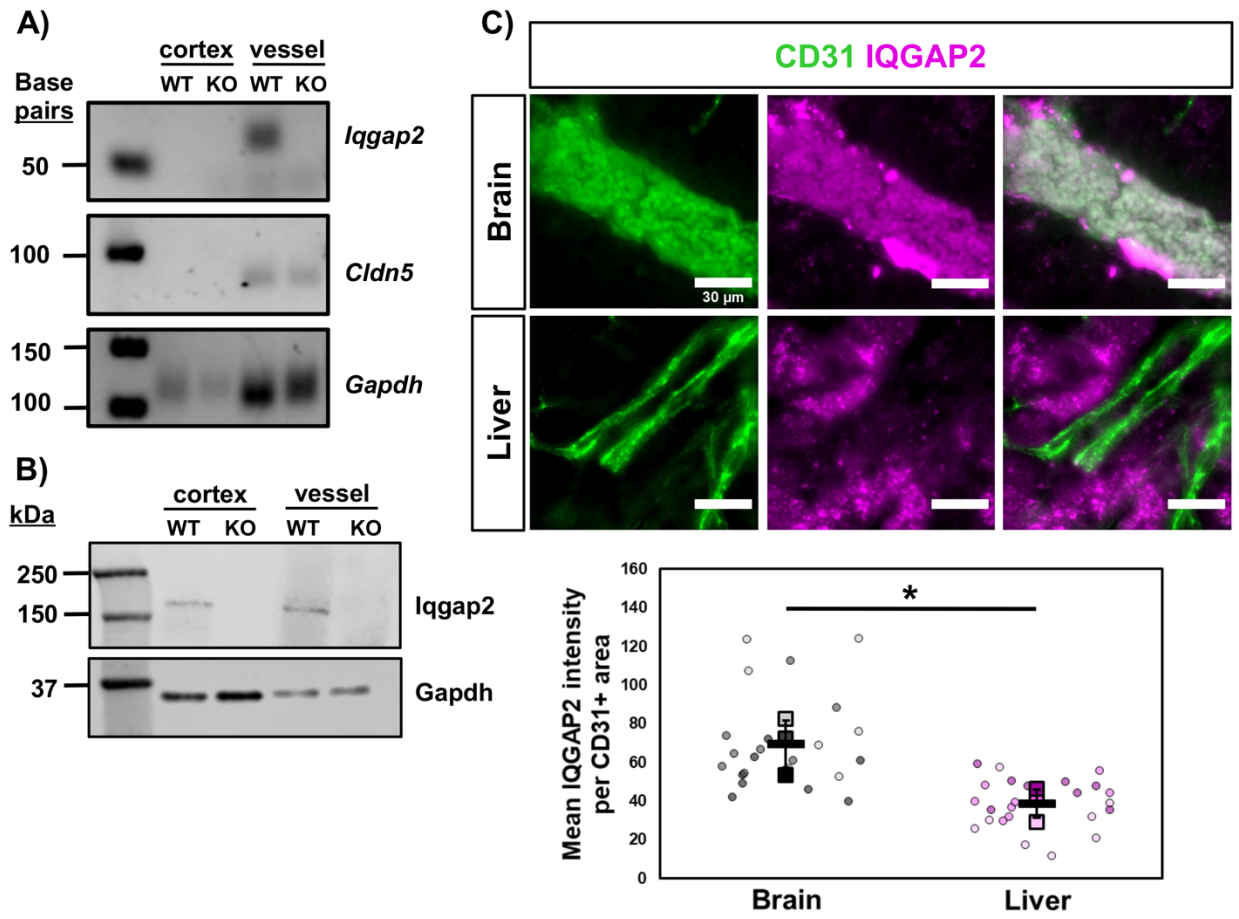

Figure 2: IQGAP2 is expressed in brain vasculature.

A) Gel electrophoresis image of PCR product bands for *Iqgap2* (60 base pairs), *Cldn5* (82 base pairs), and *Gapdh* (109 base pairs) in whole cortex and vessel fractions isolated from wild-type (WT) and Iqgap2$^{-/-}$ (KO) mice. A single sample was analyzed from 3 pooled cortex or vessel preparations.

B) Western blot images of Iqgap2 protein expression in whole cortex and vessel fractions isolated from wild-type (WT) and Iqgap2$^{-/-}$ (KO) mice. A single sample was analyzed from 3 pooled cortex or vessel preparations.

C) Representative images and quantification of vascular IQGAP2 expression in human brain cortex and human liver samples. Quantification of vascular IQGAP2 expression was performed across N=3 donor samples. Data are represented as mean ± SD (black bars).

Biological replicates are represented as squares and measurements from individual images are represented as circles color coded to each replicate. Statistical significance was calculated using the student's unpaired t-test (*, $p<0.05$).

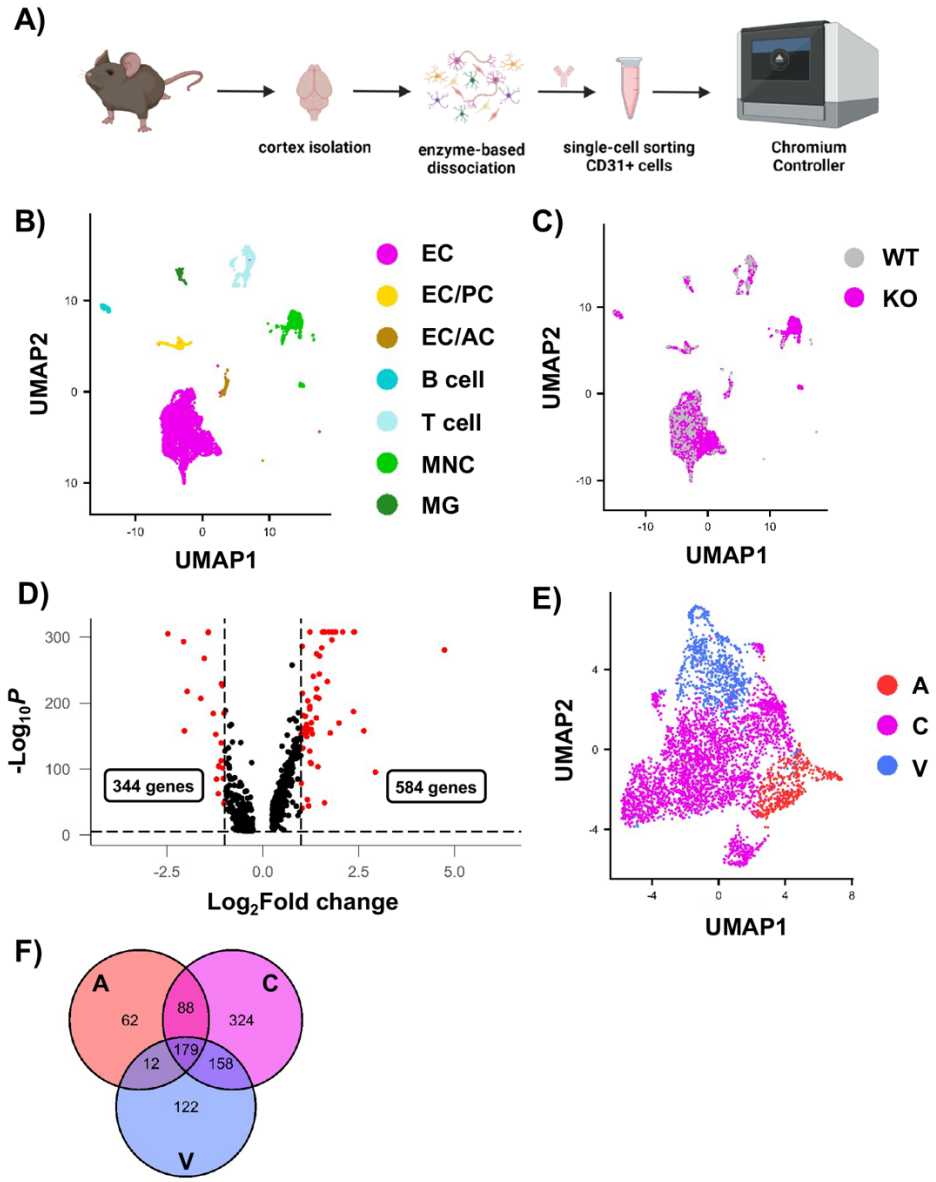

Figure 3: Global loss of Iqgap2 yields extensive transcriptional changes in BECs.

A) Schematic representation of experimental design. Whole brain cortices were isolated from wild-type (WT) and Iqgap2$^{-/-}$ (KO) mice, dissociated to a single cell suspension using enzyme-based dissociation techniques, and sorted to enrich for CD31+ cells before sequencing.

B) UMAP cell annotations based on unsupervised clustering. EC = endothelial cells, EC/PC = EC/stromal cells (pericytes), EC/AC = EC/stromal cells (astrocytes), MNC = monocytes, MG = microglia.

C) UMAP comparison between wild-type (WT, grey) and Iqgap2$^{-/-}$ (KO, pink) cells.

D) Volcano plot highlighting differentially expressed genes in the EC cluster. 928 genes were significantly altered, with 584 upregulated and 344 downregulated by loss of Iqgap2. Red dots indicate genes with $p<0.05$ and >2-fold change in expression.

E) UMAP of endothelial zonal identity based on unsupervised clustering. A = arterial, C = capillary, V = venous.

F) Venn diagram showing number of DEGs shared between zonal identities.

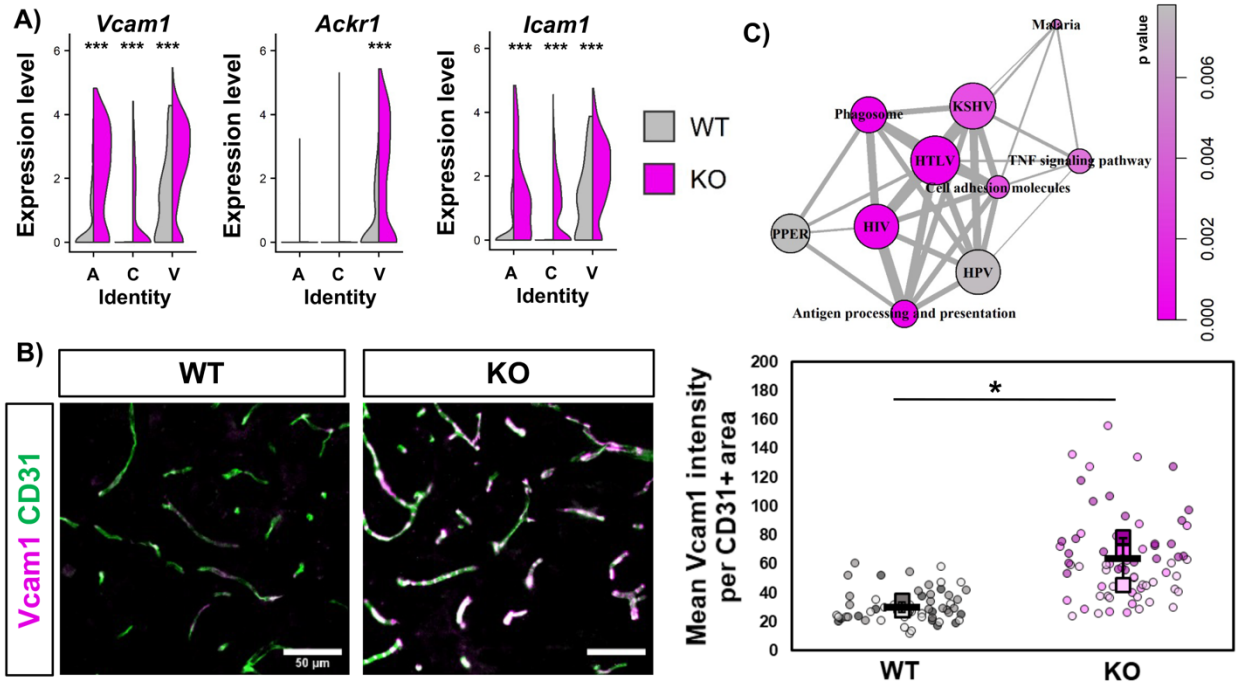

Figure 4: Global loss of Iqgap2 produces a widespread inflammatory phenotype in BECs.

A) Split violin plots indicating differential gene expression of select inflammatory markers across vascular zones. Statistical significance was calculated using Wilcox rank-order tests with Bonferroni correction (***, p<0.001).

B) Representative images and quantification of vascular Vcam1 expression in wild-type (WT) and Iqgap2$^{-/-}$ (KO) mouse cortex. Quantification of vascular Vcam-1 expression was performed across N=3 biological replicates. Data are represented as mean ± SD (black bars). Biological replicates are represented as squares and measurements from individual images are represented as circles color coded to each replicate. Statistical significance was calculated using the student's unpaired t-test (*, p<0.05).

C) GSEA pathway analysis. Each node represents an enriched gene set belonging to the labeled canonical pathway. Nodes are colored based on p-value, and thickness of the connecting lines indicates similarity of overlapping genes represented in connected gene sets. KSHV =

Kaposi sarcoma-associated herpes virus infection, HTLV = Human T-cell leukemia virus 1 infection, HIV = Human immunodeficiency virus 1 infection, PPER = Protein processing in endoplasmic reticulum, HPV = Human papillomavirus infection.

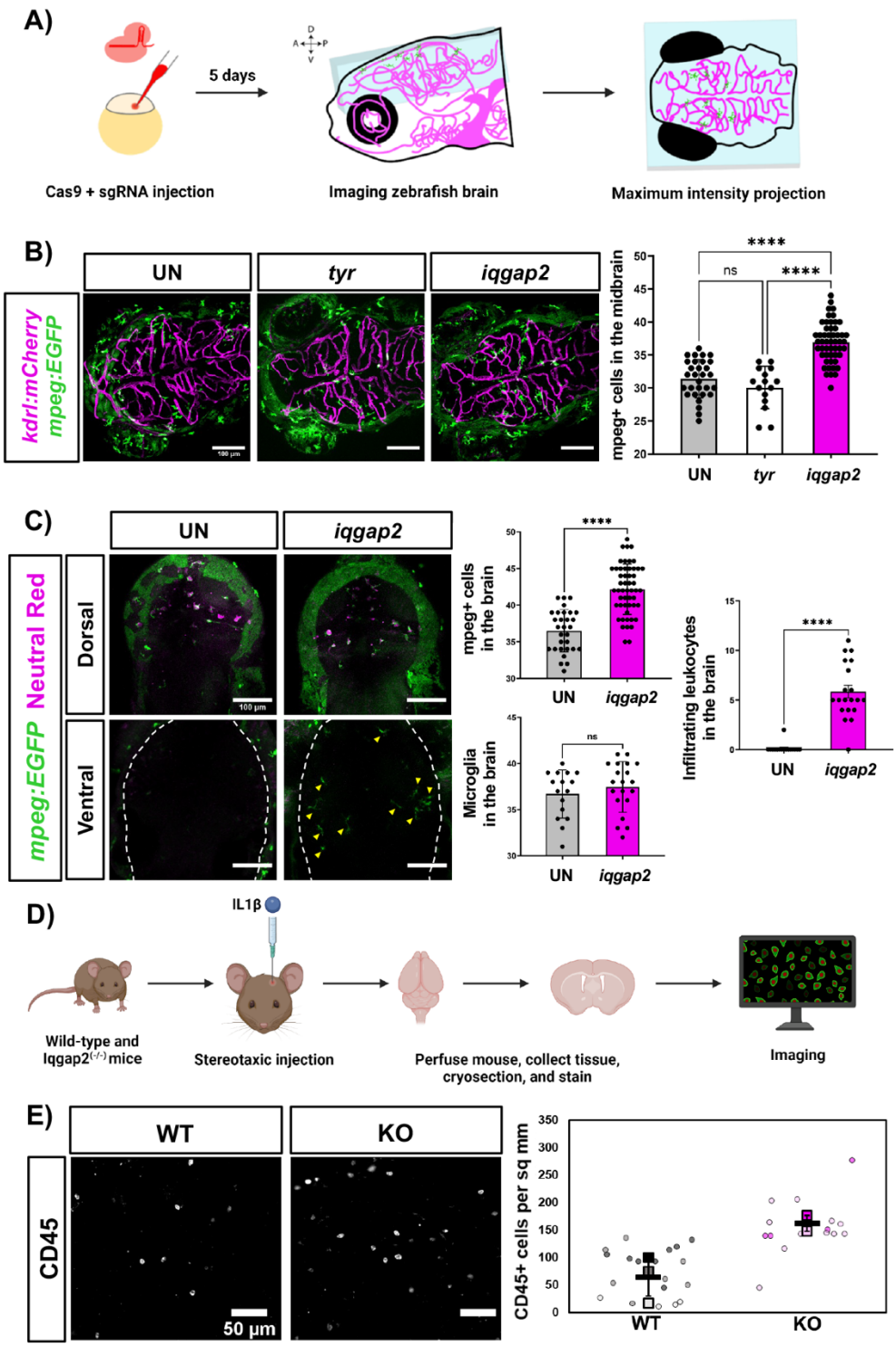

Figure 5: Loss of Iqgap2 increases infiltration of peripheral immune cells into zebrafish and mouse brain.

A) Schematic representation of experimental design for assessing leukocyte numbers in the larval zebrafish brain. Double transgenic (kdrl:mCherry; mpeg:EGFP) single-cell embryos were injected with Cas9 protein and sgRNAs to target genes of interest. These mosaic crispants were then allowed to develop normally, and leukocytes were quantified in the brain at 5 dpf in panels B-C.

B) Quantification of macrophage lineage cells (mpeg:EGFP) in the brains of *Iqgap2* crispants, *tyr* crispants, and uninjected (UN) controls. Representative 100 μm thick maximum intensity projection images are shown. Vasculature is marked with the kdrl:mCherry transgene (magenta). N=30 fish (UN), 15 fish (*tyr*), and 52 fish (*iqgap2*). Data are represented as mean ± SD, and each data point represents an individual fish. Statistical significance was calculated using a one-way ANOVA with Tukey's multiple comparison's test (****, $p<0.0001$).

C) Quantification of infiltrating leukocytes versus resident microglia in the brains of *Iqgap2* crispants versus uninjected (UN) controls. Representative 30 μm thick maximum intensity projection images of the dorsal (top) or ventral (bottom) brain regions and quantification of mpeg+ (green) macrophage lineage cells and mpeg+/Neutral Red+ (magenta). Yellow arrowheads indicate individual mpeg+/Neutral Red- infiltrating leukocytes in the ventral brain of *iqgap2* crispants. N=16 fish (UN) and 20 fish (*iqgap2*). Data represented as mean ± SD, and each data point represents an individual fish. Statistical significance was calculated using an unpaired Student's t-test (****, $p<0.0001$).

D) Schematic representation of experimental design for assessing leukocyte numbers in mouse brains 24 hours after intracerebroventricular IL1β delivery.

E) Representative images and quantification of CD45+ immune cells (white) in wild-type (WT) and Iqgap2$^{-/-}$ (KO) mouse brain cortex. Data are represented as mean ± SD (black bars). Biological replicates are represented as squares and measurements from individual images

are presented as circles color coded to each replicate (N=3 WT mice, N=2 KO mice). Statistical significance was calculated using the student's unpaired t-test (p=0.06).

References

1. Zlokovic BV. The Blood-Brain Barrier in Health and Chronic Neurodegenerative Disorders. Neuron. 2008;57:178–201.

2. Profaci CP, Munji RN, Pulido RS, Daneman R. The blood–brain barrier in health and disease: Important unanswered questions. J Exp Med. 2020;217:e20190062.

3. Daneman R, Prat A. The Blood–Brain Barrier. Cold Spring Harb Perspect Biol. 2015;7:a020412.

4. Obermeier B, Daneman R, Ransohoff RM. Development, maintenance and disruption of the blood-brain barrier. Nat Med. 2013;19:1584–96.

5. Engelhardt B, Coisne C. Fluids and barriers of the CNS establish immune privilege by confining immune surveillance to a two-walled castle moat surrounding the CNS castle. Fluids Barriers CNS. 2011;8:4.

6. Louveau A, Harris TH, Kipnis J. Revisiting the Mechanisms of CNS Immune Privilege. Trends Immunol. 2015;36:569–77.

7. Engelhardt B, Vajkoczy P, Weller RO. The movers and shapers in immune privilege of the CNS. Nat Immunol. 2017;18:123–31.

8. Marchetti L, Engelhardt B. Immune cell trafficking across the blood-brain barrier in the absence and presence of neuroinflammation. Vasc Biol. 2020;2:H1–18.

9. Mapunda JA, Tibar H, Regragui W, Engelhardt B. How Does the Immune System Enter the Brain? Front Immunol. 2022;13:805657.

10. Raivich G. Like cops on the beat: the active role of resting microglia. Trends Neurosci. 2005;28:571–3.

11. Ousman SS, Kubes P. Immune surveillance in the central nervous system. Nat Neurosci. 2012;15:1096–101.

12. Laman JD, Weller RO. Drainage of Cells and Soluble Antigen from the CNS to Regional Lymph Nodes. J Neuroimmune Pharmacol. 2013;8:840–56.

13. Louveau A, Plog BA, Antila S, Alitalo K, Nedergaard M, Kipnis J. Understanding the functions and relationships of the glymphatic system and meningeal lymphatics. J Clin Invest. 2017;127:3210–9.

14. Engelhardt B, Carare RO, Bechmann I, Flügel A, Laman JD, Weller RO. Vascular, glial, and lymphatic immune gateways of the central nervous system. Acta Neuropathol (Berl). 2016;132:317–38.

15. das Neves SP, Delivanoglou N, Da Mesquita S. CNS-Draining Meningeal Lymphatic Vasculature: Roles, Conundrums and Future Challenges. Front Pharmacol. 2021;12:655052.

16. Engelhardt B, Ransohoff RM. The ins and outs of T-lymphocyte trafficking to the CNS: anatomical sites and molecular mechanisms. Trends Immunol. 2005;26:485–95.

17. Engelhardt B, Ransohoff RM. Capture, crawl, cross: the T cell code to breach the blood–brain barriers. Trends Immunol. 2012;33:579–89.

18. Aydin S, Pareja J, Schallenberg VM, Klopstein A, Gruber T, Page N, et al. Brain endothelial antigen presentation detains CD8 $^{+}$ T cells at the blood-brain barrier leading to its breakdown [Internet]. Immunology; 2021 Oct. Available from: http://biorxiv.org/lookup/doi/10.1101/2021.10.12.464035

19. Fain C, Zheng J, Jin F, Ayasoufi K, Wu Y, Lilley M, et al. Antigen presentation by discrete class I molecules on brain endothelium dynamically regulates T-cell mediated neuropathology in experimental cerebral malaria [Internet]. Neuroscience; 2022 Nov. Available from: http://biorxiv.org/lookup/doi/10.1101/2022.10.30.514412

20. Lopes Pinheiro MA, Kamermans A, Garcia-Vallejo JJ, van het Hof B, Wierts L, O'Toole T, et al. Internalization and presentation of myelin antigens by the brain endothelium guides antigen-specific T cell migration. eLife. 2016;5:e13149.

21. Galea I. The blood–brain barrier in systemic infection and inflammation. Cell Mol Immunol. 2021;18:2489–501.

22. Vanlandewijck M, He L, Mäe MA, Andrae J, Ando K, Del Gaudio F, et al. A molecular atlas of cell types and zonation in the brain vasculature. Nature. 2018;554:475–80.

23. Sabbagh MF, Heng JS, Luo C, Castanon RG, Nery JR, Rattner A, et al. Transcriptional and epigenomic landscapes of CNS and non-CNS vascular endothelial cells. eLife. 2018;7:e36187.

24. Kalucka J, de Rooij LPMH, Goveia J, Rohlenova K, Dumas SJ, Meta E, et al. Single-Cell Transcriptome Atlas of Murine Endothelial Cells. Cell. 2020;180:764-779.e20.

25. Yang AC, Vest RT, Kern F, Lee DP, Agam M, Maat CA, et al. A human brain vascular atlas reveals diverse mediators of Alzheimer's risk. Nature. 2022;603:885–92.

26. Garcia FJ, Sun N, Lee H, Godlewski B, Mathys H, Galani K, et al. Single-cell dissection of the human brain vasculature. Nature. 2022;603:893–9.

27. Winkler EA, Kim CN, Ross JM, Garcia JH, Gil E, Oh I, et al. A single-cell atlas of the normal and malformed human brain vasculature. Science. 2022;375:eabi7377.

28. White CD, Brown MD, Sacks DB. IQGAPs in cancer: A family of scaffold proteins underlying tumorigenesis. FEBS Lett. 2009;583:1817–24.

29. Yanyun Xie, Anil Kapoor, Hao Peng, Jean-Claude Cutz, Lijian Tao, Damu Tang. IQGAP2 Displays Tumor Suppression Functions. J Anal Oncol [Internet]. 2015 [cited 2023 Jan 25];4. Available from: https://neoplasiaresearch.com/pms/index.php/jao/article/view/249

30. Dai Q, Ain Q, Rooney M, Song F, Zipprich A. Role of IQ Motif-Containing GTPase-Activating Proteins in Hepatocellular Carcinoma. Front Oncol. 2022;12:920652.

31. Lippmann ES, Azarin SM, Kay JE, Nessler RA, Wilson HK, Al-Ahmad A, et al. Derivation of blood-brain barrier endothelial cells from human pluripotent stem cells. Nat Biotechnol. 2012;30:783–91.

32. Hollmann EK, Bailey AK, Potharazu AV, Neely MD, Bowman AB, Lippmann ES. Accelerated differentiation of human induced pluripotent stem cells to blood–brain barrier endothelial cells. Fluids Barriers CNS. 2017;14:9.

33. Neal EH, Marinelli NA, Shi Y, McClatchey PM, Balotin KM, Gullett DR, et al. A Simplified, Fully Defined Differentiation Scheme for Producing Blood-Brain Barrier Endothelial Cells from Human iPSCs. Stem Cell Rep. 2019;12:1380–8.

34. Neal EH, Katdare KA, Shi Y, Marinelli NA, Hagerla KA, Lippmann ES. Influence of basal media composition on barrier fidelity within human pluripotent stem cell-derived blood-brain barrier models. J Neurochem. 2021;159:980–91.

35. Lippmann ES, Al-Ahmad A, Azarin SM, Palecek SP, Shusta EV. A retinoic acid-enhanced, multicellular human blood-brain barrier model derived from stem cell sources. Sci Rep. 2015;4:4160.

36. Stebbins MJ, Lippmann ES, Faubion MG, Daneman R, Palecek SP, Shusta EV. Activation of RARα, RARγ, or RXRα Increases Barrier Tightness in Human Induced Pluripotent Stem Cell-Derived Brain Endothelial Cells. Biotechnol J. 2018;13:1700093.

37. Sabbagh MF, Nathans J. A genome-wide view of the de-differentiation of central nervous system endothelial cells in culture. eLife. 2020;9:e51276.

38. He L, Vanlandewijck M, Mäe MA, Andrae J, Ando K, Del Gaudio F, et al. Single-cell RNA sequencing of mouse brain and lung vascular and vessel-associated cell types. Sci Data. 2018;5:180160.

39. Saliba A-E, Westermann AJ, Gorski SA, Vogel J. Single-cell RNA-seq: advances and future challenges. Nucleic Acids Res. 2014;42:8845–60.

40. Sullivan DP, Dalal PJ, Jaulin F, Sacks DB, Kreitzer G, Muller WA. Endothelial IQGAP1 regulates leukocyte transmigration by directing the LBRC to the site of diapedesis. J Exp Med. 2019;216:2582–601.

41. Sullivan DP, Dalal PJ, Sacks DB, Muller WA. Calcium Signaling Regulates Leukocyte Transendothelial Migration through the Action of Endothelial Cell IQGAP1, Calmodulin, and CaMKIIδ. FASEB J. 2020;34:1–1.

42. White CD, Khurana H, Gnatenko DV, Li Z, Odze RD, Sacks DB, et al. IQGAP1 and IQGAP2 are Reciprocally Altered in Hepatocellular Carcinoma. BMC Gastroenterol. 2010;10:125.

43. Smith JM, Hedman AC, Sacks DB. IQGAPs choreograph cellular signaling from the membrane to the nucleus. Trends Cell Biol. 2015;25:171–84.

44. Zhao L, Li Z, Vong JSL, Chen X, Lai H-M, Yan LYC, et al. Pharmacologically reversible zonation-dependent endothelial cell transcriptomic changes with neurodegenerative disease associations in the aged brain. Nat Commun. 2020;11:4413.

45. Rossi B, Angiari S, Zenaro E, Budui SL, Constantin G. Vascular inflammation in central nervous system diseases: adhesion receptors controlling leukocyte-endothelial interactions. J Leukoc Biol. 2011;89:539–56.

46. Muller WA. Getting Leukocytes to the Site of Inflammation. Vet Pathol. 2013;50:7–22.

47. Nourshargh S, Alon R. Leukocyte Migration into Inflamed Tissues. Immunity. 2014;41:694–707.

48. Ben-Zvi A, Lacoste B, Kur E, Andreone BJ, Mayshar Y, Yan H, et al. Mfsd2a is critical for the formation and function of the blood–brain barrier. Nature. 2014;509:507–11.

49. Daneman R, Agalliu D, Zhou L, Kuhnert F, Kuo CJ, Barres BA. Wnt/β-catenin signaling is required for CNS, but not non-CNS, angiogenesis. Proc Natl Acad Sci. 2009;106:641–6.

50. Stenman JM, Rajagopal J, Carroll TJ, Ishibashi M, McMahon J, McMahon AP. Canonical Wnt Signaling Regulates Organ-Specific Assembly and Differentiation of CNS Vasculature. Science. 2008;322:1247–50.

51. Liebner S, Corada M, Bangsow T, Babbage J, Taddei A, Czupalla CJ, et al. Wnt/β-catenin signaling controls development of the blood–brain barrier. J Cell Biol. 2008;183:409–17.

52. Yousef H, Czupalla CJ, Lee D, Chen MB, Burke AN, Zera KA, et al. Aged blood impairs hippocampal neural precursor activity and activates microglia via brain endothelial cell VCAM1. Nat Med. 2019;25:988–1000.

53. Kim H, Leng K, Park J, Sorets AG, Kim S, Shostak A, et al. Reactive astrocytes transduce inflammation in a blood-brain barrier model through a TNF-STAT3 signaling axis and secretion of alpha 1-antichymotrypsin. Nat Commun. 2022;13:6581.

54. Jin S, Guerrero-Juarez CF, Zhang L, Chang I, Ramos R, Kuan C-H, et al. Inference and analysis of cell-cell communication using CellChat. Nat Commun. 2021;12:1088.

55. Shiau CE, Monk KR, Joo W, Talbot WS. An Anti-inflammatory NOD-like Receptor Is Required for Microglia Development. Cell Rep. 2013;5:1342–52.

56. Proescholdt MG, Chakravarty S, Foster JA, Foti SB, Briley EM, Herkenham M. Intracerebroventricular but not intravenous interleukin-1β induces widespread vascular-mediated leukocyte infiltration and immune signal mRNA expression followed by brain-wide glial activation. Neuroscience. 2002;112:731–49.

57. Liu X, Nemeth DP, McKim DB, Zhu L, DiSabato DJ, Berdysz O, et al. Cell-Type-Specific Interleukin 1 Receptor 1 Signaling in the Brain Regulates Distinct Neuroimmune Activities. Immunity. 2019;50:764–6.

58. Bevilacqua MP. Endothelial-Leukocyte Adhesion Molecules. Annu Rev Immunol. 1993;11:767–804.

59. Hickey WF, Hsu BL, Kimura H. T-lymphocyte entry into the central nervous system. J Neurosci Res. 1991;28:254–60.

60. Rössler K, Neuchrist C, Kitz K, Scheiner O, Kraft D, Lassmann H. Expression of leucocyte adhesion molecules at the human blood-brain barrier (BBB). J Neurosci Res. 1992;31:365–74.

61. Yilmaz G, Granger DN. Cell adhesion molecules and ischemic stroke. Neurol Res. 2008;30:783–93.

62. Amor S, Puentes F, Baker D, van der Valk P. Inflammation in neurodegenerative diseases. Immunology. 2010;129:154–69.

63. Roberts TK. Leukocyte transmigration across the blood-brain barrier: perspectives on neuroAIDS. Front Biosci. 2010;15:478.

64. Dulken BW, Buckley MT, Navarro Negredo P, Saligrama N, Cayrol R, Leeman DS, et al. Single-cell analysis reveals T cell infiltration in old neurogenic niches. Nature. 2019;571:205–10.

65. Gate D, Saligrama N, Leventhal O, Yang AC, Unger MS, Middeldorp J, et al. Clonally expanded CD8 T cells patrol the cerebrospinal fluid in Alzheimer's disease. Nature. 2020;577:399–404.

66. Chen MB, Yang AC, Yousef H, Lee D, Chen W, Schaum N, et al. Brain Endothelial Cells Are Exquisite Sensors of Age-Related Circulatory Cues. Cell Rep. 2020;30:4418-4432.e4.

67. Hedman AC, Smith JM, Sacks DB. The biology of IQGAP proteins: beyond the cytoskeleton. EMBO Rep. 2015;16:427–46.

68. Xu L, Shao Y, Ren L, Liu X, Li Y, Xu J, et al. IQGAP2 Inhibits Migration and Invasion of Gastric Cancer Cells via Elevating SHIP2 Phosphatase Activity. Int J Mol Sci. 2020;21:1968.

69. Xie Y, Zheng L, Tao L. Downregulation of IQGAP2 Correlates with Prostate Cancer Recurrence and Metastasis. Transl Oncol. 2019;12:236–44.

70. Song F, Kotolloshi R, Gajda M, Hölzer M, Grimm M-O, Steinbach D. Reduced IQGAP2 Promotes Bladder Cancer through Regulation of MAPK/ERK Pathway and Cytokines. Int J Mol Sci. 2022;23:13508.

71. Dai Q, Song F, Li X, Huang F, Zhao H. Comprehensive analysis of the expression and prognosis for IQ motif-containing GTPase-activating proteins in hepatocellular carcinoma. BMC Cancer. 2022;22:1121.

72. Deng Z, Wang L, Hou H, Zhou J, Li X. Epigenetic regulation of IQGAP2 promotes ovarian cancer progression via activating Wnt/β-catenin signaling. Int J Oncol. 2016;48:153–60.

73. Hayashi H, Nabeshima K, Aoki M, Hamasaki M, Enatsu S, Yamauchi Y, et al. Overexpression of IQGAP1 in advanced colorectal cancer correlates with poor prognosis-critical role in tumor invasion. Int J Cancer. 2010;NA-NA.

74. Jin X, Liu Y, Liu J, Lu W, Liang Z, Zhang D, et al. The Overexpression of IQGAP1 and β-Catenin Is Associated with Tumor Progression in Hepatocellular Carcinoma In Vitro and In Vivo. Samant R, editor. PLOS ONE. 2015;10:e0133770.

75. Hu W, Wang Z, Zhang S, Lu X, Wu J, Yu K, et al. IQGAP1 promotes pancreatic cancer progression and epithelial-mesenchymal transition (EMT) through Wnt/β-catenin signaling. Sci Rep. 2019;9:7539.

76. Schmidt VA, Chiariello CS, Capilla E, Miller F, Bahou WF. Development of Hepatocellular Carcinoma in *Iqgap2* -Deficient Mice Is IQGAP1 Dependent. Mol Cell Biol. 2008;28:1489–502.

77. Lengfeld JE, Lutz SE, Smith JR, Diaconu C, Scott C, Kofman SB, et al. Endothelial Wnt/β-catenin signaling reduces immune cell infiltration in multiple sclerosis. Proc Natl Acad Sci [Internet]. 2017 [cited 2022 Sep 21];114. Available from: https://pnas.org/doi/full/10.1073/pnas.1609905114

78. Kumar KK, Lowe, EW, Aboud AA, Neely MD, Redha R, Bauer JA, et al. Cellular manganese content is developmentally regulated in human dopaminergic neurons. Sci Rep. 2015;4:6801.

79. Chen G, Gulbranson DR, Hou Z, Bolin JM, Ruotti V, Probasco MD, et al. Chemically defined conditions for human iPSC derivation and culture. Nat Methods. 2011;8:424–9.

80. Westerfield M. The zebrafish book: a guide for the laboratory use of zebrafish (Brachydanio rerio). 1993.

81. Chi NC, Shaw RM, De Val S, Kang G, Jan LY, Black BL, et al. Foxn4 directly regulates tbx2b expression and atrioventricular canal formation. Genes Dev. 2008;22:734–9.

82. Ellett F, Pase L, Hayman JW, Andrianopoulos A, Lieschke GJ. mpeg1 promoter transgenes direct macrophage-lineage expression in zebrafish. Blood. 2011;117:e49-56.

83. Lee Y-K, Uchida H, Smith H, Ito A, Sanchez T. The isolation and molecular characterization of cerebral microvessels. Nat Protoc. 2019;14:3059–81.

84. Köster J, Rahmann S. Snakemake—a scalable bioinformatics workflow engine. Bioinformatics. 2012;28:2520–2.

85. Love MI, Huber W, Anders S. Moderated estimation of fold change and dispersion for RNA-seq data with DESeq2. Genome Biol. 2014;15:550.

86. Becht E, McInnes L, Healy J, Dutertre C-A, Kwok IWH, Ng LG, et al. Dimensionality reduction for visualizing single-cell data using UMAP. Nat Biotechnol. 2019;37:38–44.

87. McGinnis CS, Murrow LM, Gartner ZJ. DoubletFinder: Doublet Detection in Single-Cell RNA Sequencing Data Using Artificial Nearest Neighbors. Cell Syst. 2019;8:329-337.e4.

88. Stuart T, Butler A, Hoffman P, Hafemeister C, Papalexi E, Mauck WM, et al. Comprehensive Integration of Single-Cell Data. Cell. 2019;177:1888-1902.e21.

89. Aran D, Looney AP, Liu L, Wu E, Fong V, Hsu A, et al. Reference-based analysis of lung single-cell sequencing reveals a transitional profibrotic macrophage. Nat Immunol. 2019;20:163–72.

90. Liao Y, Wang J, Jaehnig EJ, Shi Z, Zhang B. WebGestalt 2019: gene set analysis toolkit with revamped UIs and APIs. Nucleic Acids Res. 2019;47:W199–205.

91. Blighe K, Rana S, Lewis M. EnhancedVolcano: publication-ready volcano plots with enhanced colouring and labeling [Internet]. 2018. Available from: https://bioconductor.org/packages/release/bioc/vignettes/EnhancedVolcano/inst/doc/EnhancedVolcano.html

92. Lex A, Gehlenborg N, Strobelt H, Vuillemot R, Pfister H. UpSet: Visualization of Intersecting Sets. IEEE Trans Vis Comput Graph. 2014;20:1983–92.

93. Csardi G, Nepusz T. The igraph software package for complex network research. InterJournal. 2006;Complex Systems:1695.